Recursive Estimation of Spacecraft Position Using X-ray Pulsar Time of Arrival Measurements

Suneel I. Sheikh and Darryll J. Pines, *The University of Maryland*

BIOGRAPHY

Mr. Sheikh is a PhD student in the Aerospace Engineering Department of the University of Maryland. His doctoral research investigates the use of X-ray pulsars for spacecraft navigation. Prior to this, Mr. Sheikh has over ten years of industry experience in the field of INS and GPS integration and research.

Dr. Pines is a Professor in the Aerospace Engineering Department of the University of Maryland. His research includes spacecraft navigation, structural dynamics, vehicle health monitoring, and micro air vehicle development. Dr. Pines is currently on leave as a Program Manager at DARPA.

ABSTRACT

The use of pulsars for spacecraft position determination has been considered since their discovery [1-3]. These celestial sources provide unique signals that can be detected by sensors placed onboard spacecraft. Upon sufficient detection and processing, these signals can be used to generate range measurements with respect to an inertial reference location. Multiple measurements can be used to determine a navigation solution and enhance autonomous vehicle operation. This paper provides a description of blending pulsar-derived range measurements within a Kalman filter for Earth-orbiting spacecraft navigation. Several examples at different orbital altitudes are presented to determine the expected navigation performance using recursive measurements obtained from models of pulsed X-ray signals.

INTRODUCTION

Spacecraft in orbit about Earth follow predictable, often stable, paths that can be estimated using a numerical propagator of the vehicle's dynamics. However, unmodeled or unforeseen disturbances may perturb the vehicle from the orbit path and eventually the numerical propagator's estimated position would grow to an unacceptable level for vehicle guidance or control. Orbit determination methods using observations of the spacecraft from Earth ground stations can detect these deviations of the vehicle from the predicted path and can update the estimation of the orbital elements. However, increased autonomy of vehicle operation, and perhaps reduced costs, are achieved if the spacecraft's navigation system can detect these deviations and correct its own solution without input from ground stations. Using external aids, the system can update its estimate of position and velocity in order to maintain a desired performance. Celestial sources have proven to be significant aids for navigation throughout history. Recently discovered pulsars are a subset of celestial sources, which can be shown to provide new benefits to spacecraft navigation [4].

Rotation-powered pulsars are theorized to be rotating neutron stars that emit electromagnetic radiation along their magnetic field axis [5, 6]. As the star rotates about its spin axis, the radiation appears to *pulse* towards an observer as the magnetic pole sweeps past the observer's line of sight to the star. The pulsations from many of these sources have been shown to be very stable and predictable [7, 8]. These stars emit pulsed, or variable, radiation in all bands of the electromagnetic spectrum, however detection within the X-ray band allows for the development of more compact detectors than other bands, including radio and optical. There are several types of variable X-ray celestial sources, but pulsars, with their stable, periodic, predictable signatures, are the most attractive for use in position determination [9].

In addition to rotation-powered pulsars, *accretion-powered pulsars* exist, which emit pulsed radiation through the changing viewing angle of thermal hot spots on their surface created by the accretion of material from their companion within a binary system [5, 6]. These types of pulsars also show signal stability and predictability. Although they possess complicated pulse timing models due to their binary system dynamics, and many are transient sources with unpredictable durations

of low signal intensity, these types of pulsars also have characteristics conducive to navigation.

The periodic pulsations from these sources essentially emulate celestial *lighthouses*, or *clocks,* and can be used as navigation beacons in methods similar to Earth-based navigation systems, such as the Global Positioning System (GPS) and the Global Orbiting Navigation Satellite System (GLONASS). Pulsars are extremely distant from the solar system, which provides good visibility of their signal near Earth as well as throughout the solar system. However, unlike GPS or GLONASS, the distances of these sources cannot be measured such that direct range measurements from the sources can be determined. Rather, indirect range measurement along the line of sight to a pulsar from a reference location to a spacecraft can be computed. Recent studies have presented these concepts, as well as demonstrated some preliminary experimental results [10, 11]. Presented here is the use of these range measurements to recursively update, or correct, the position of a spacecraft in orbit about Earth to provide a continuous, accurate navigation solution. Several orbits are investigated, including spacecraft in LEO, MEO, and GPS orbits, as well as orbits about Earth's Moon.

SOURCE CHARACTERIZATION

The cyclic emissions generated by variable celestial sources offer measurable signals that can be utilized within a navigation system. In order to use these signals, they must be detectable, such that sensors can be developed to determine the arrival of the emissions from each individual unique source; the signals must be able to be characterized, such that the necessary distinctive parameters of a specific source can be resolved and be used to identify each source as data are recorded; and the signals must be able to be modeled, such that methods can be created to predict the future arrival time of the signals at a given location.

At X-ray energy wavelengths, the measured components of the emitted signal from a source are the individual photons released in the energy discharge. An observed profile is created via the detection of these photons from the source as they arrive at the navigation system's detector. The number of photons detected within a given observation spans numerous pulse cycles if the observation time is much greater than the pulse cycle period. Each photon is a component of an individual pulse, and detecting a single photon does not immediately provide an indication of a given pulse.

The process of assembling all the measured photon events into a pulse profile is referred to as *epoch folding*, or averaging synchronously all the photon events with the expected pulse period of the source. The resulting histogram of photon arrivals over the pulse cycle length renders the profile of the pulse from the source. Once produced, characteristics of the pulse can be determined from a profile, or set of profiles. These characteristics include pulse amplitude above the averaged signal, and number and shape of peaks. Variability in parameters such as period length and noise, as well as continuity of pulsed emission can be determined. The unique characteristics of each source's pulse profile aids in the identification process of the source.

Standard template profiles are produced similarly to observation profiles however, these templates utilize much longer observation times and possibly multiple observations folded together in order to gain a very high signal-to-noise ratio (SNR) value. Figure 1 shows a standard pulse template for the Crab Pulsar (PSR B0531+21) in the X-ray band (1–15 keV) created using multiple observations with the Unconventional Stellar Aspect (USA) experiment produced by the Naval Research Laboratory (NRL) as it operated onboard the Advanced Research and Global Observation satellite (ARGOS) [12]. The intensity of the profile is a ratio of count rate relative to average count rate. This image shows two pulse cycles for clarity. The Crab Pulsar's pulse is comprised of one main pulse and smaller secondary sub-pulse with lower intensity amplitude.

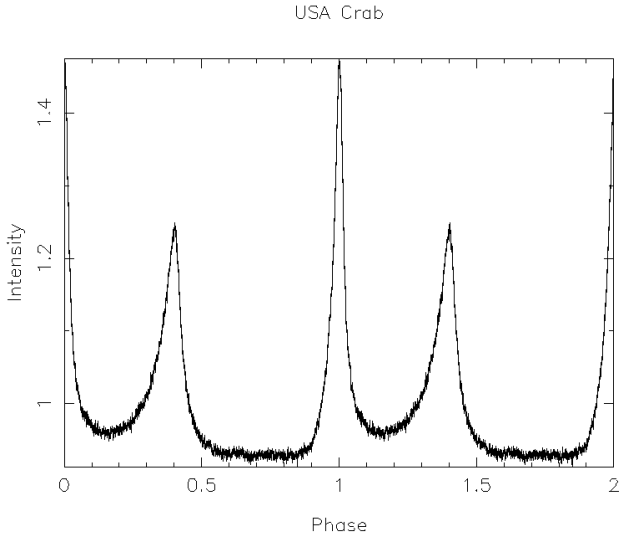

Figure 1. Crab pulsar standard pulse template profile.

The fundamental measurable quantity for time and position determination within a variable source-based navigation system is the arrival time of an observed pulse at the detector. It is necessary to determine the time of arrival (TOA) of the pulse so that navigation algorithms can compute comparisons of the measured TOA to the predicted TOA. A TOA is computed by comparing observed and standard template profiles. An observed profile, $p(t)$, will differ from the template profile, $s(t)$, by several factors. Typically the observed pulse will vary

by a shift of time origin, Δt_S, a bias, b, a scale factor, k, and random noise $\eta(t)$ [13, 14]. The relationship between the observed profile and the template profile is given by,

$$p(t) = b + k\left[s\left(t - \Delta t_S\right)\right] + \eta(t) \quad (1)$$

For X-ray observations that record individual photon events, Poisson counting statistics typically dominates the random noise in this expression. The time shift necessary to align the peaks within the two profiles is added to the start time of the observation to produce the TOA of the pulse for a particular observation.

The pulsed emission from variable celestial sources arrives within the solar system with sufficient regularity that the arrival of each pulse can be modeled. These models predict when specific pulses from the sources will arrive within the solar system. Pulse timing models are often represented as the total accumulated phase of the source's signal as a function of time. A starting cycle number, $\Phi_0 = \Phi(t_0)$, can be arbitrarily assigned to the pulse that arrives at a fiducial time, t_0, and all subsequent pulses are numbered incrementally from this first pulse. The phase of arriving pulses, Φ, is measured as the sum of the fractions of the period, or phase fraction, ϕ, and the accumulated whole value cycles, N. These can be expressed as functions of time as,

$$\Phi(t) = \phi(t) + N(t) \quad (2)$$

Using the determined pulse frequency, f, and its derivatives, the total phase can be specified at a specific location using a pulsar phase model of,

$$\Phi(t) = \Phi(t_0) + f\left[t - t_0\right] + \frac{\dot{f}}{2}\left[t - t_0\right]^2 + \frac{\ddot{f}}{6}\left[t - t_0\right]^3 \quad (3)$$

Eq. (3) is known as the *pulsar spin equation*, or *pulsar spin down law* [5, 6]. In this equation, the observation time, t, is in *coordinate time* of the pulse TOA.

Since the pulse phase depends on the time when it is measured as well as the position in space where it is measured, the pulse-timing model must also be defined for a specific location in space. Therefore along with the parameters that define the model, the location of where this model is valid must also be supplied for accurate pulsar timing. Typically, the location is chosen as the solar system barycenter (SSB), or center of mass, because of its benefits as an inertial frame origin. However, other locations can be used if they are defined with the model.

As select sources have had extended observations over many years, the stability of spin rates of some of these sources compares well with today's atomic clocks [7, 8]. This high stability allows for accurate pulse prediction and timing models.

The estimated accuracy of this arrival time measurement is an important aspect for navigation. This accuracy is used to weigh the processing of each TOA either in a batch estimation process or Kalman filter implementation to improve solutions of spacecraft navigation data. It is important to determine the TOA with an accuracy that is determined by the SNR of the profile, and not by the choice of the phase bin size. A standard cross-correlation analysis does not allow this to be easily achieved. However, the method given by Taylor [14] is independent of bin size and can be implemented into a navigation system. This method computes TOA accuracy based upon the observed profile characteristics compared to the template profile using Fourier transform analysis.

An alternative method for estimating accuracy, used here, computes the SNR of a source based upon the known X-ray characteristics of the source, the photon collection area of the detector, A, and the total observation time, t_{obs}. The pulsed fraction, p_f, defines the percentage of the source flux that is pulsed. The noise of the pulsed signal is comprised of a fraction of both the background radiation flux, B_X, and the total observed flux from this source, F_X. The background flux and the non-pulsed component of the signal contribute to the noise during the duty cycle of the pulse [15, 16]. The pulsed signal contribution to the noise exists throughout the full pulse period. The *duty cycle*, d, of a pulse is the fraction that the width of the pulse, W, spans the pulse period, P, as $d = W/P$. Using this representation of signal noise, the SNR can be determined using the ratio of pulsed component of the signal source photon counts, $N_{S_{pulsed}}$, to the one sigma error in detecting this signal as [11, 15, 16],

$$SNR = \frac{N_{S_{pulsed}}}{\sigma_{noise}} = \frac{N_{S_{pulsed}}}{\sqrt{\left(N_B + N_{S_{non-pulsed}}\right)_{duty\,cycle} + N_{S_{pulsed}}}} = \frac{F_X A p_f t_{obs}}{\sqrt{\left(B_X + F_X\left(1 - p_f\right)\right)\left(A t_{obs} d\right) + F_X A p_f t_{obs}}} \quad (4)$$

For an observation, the TOA accuracy can be determined from the one-sigma value of the pulse and the SNR via,

$$\sigma_{TOA} = \frac{\frac{1}{2}W}{SNR} \quad (5)$$

In this equation, the one-sigma value of the pulse has been estimated as one-half the pulse width (or Half-Width Half Maximum, HWHM), which assumes the pulse shape is approximately Gaussian and the full width is equal to two-sigma. The TOA accuracy represents the resolution of the arrival time of a pulse based upon a single observation. A TOA measurement can be used to determine range of the detector from a chosen reference location along the line of sight to the pulsar. The accuracy of a range measurement can be computed using the speed of light, c, and the pulse TOA accuracy from Eq. (5) as,

$$\sigma_{range} = c\,\sigma_{TOA} \quad (6)$$

Although numerous pulsars have been discovered, detailed analysis and characterization of many of these is ongoing. Three important pulsar sources and their parameters are provided in Table 1 and Table 2, listed in increasing pulse period. These sources were chosen as representative candidate navigation sources due to their extensive study and their potential benefits of creating accurate navigation solutions.

Table 1. Pulsar Position and References.

Name (PSR)	Galactic Longitude (deg)	Galactic Latitude (deg)	Dist. (kpc)	Refs.
B1937+21	57.51	-0.29	3.60	[17, 18]
B1821–24	7.80	-5.58	5.50	[17, 19]
B0531+21	184.56	-5.78	2.00	[17, 19]

Table 2. Pulsar Period and Characteristics.

Name (PSR)	Period (s)	Flux 2–10 keV (ph/cm^2/s)	Pulsed Frac. (%)	Pulse Width (s)
B1937+21	0.00156	4.99E-05	86.0	0.000021
B1821–24	0.00305	1.93E-04	98.0	0.000055
B0531+21	0.03340	1.54E+00	70.0	0.001670

Using the data of pulsar parameters in Table 1 and Table 2, plots of achievable range accuracy can be created. For these plots, a common X-ray background rate of 0.005 ph/cm^2/s over 2–10 keV energy range was used for each source, and the detector area was chosen as 1-m^2. Assuming unlimited values of SNR > 2, Figure 2 presents the range accuracy of each source based upon total observation duration. Table 3 lists the values of the accuracy at selected observation durations. Both the plot in this figure and the data in the table assume that SNR is unbounded, which may not be true for all pulsars.

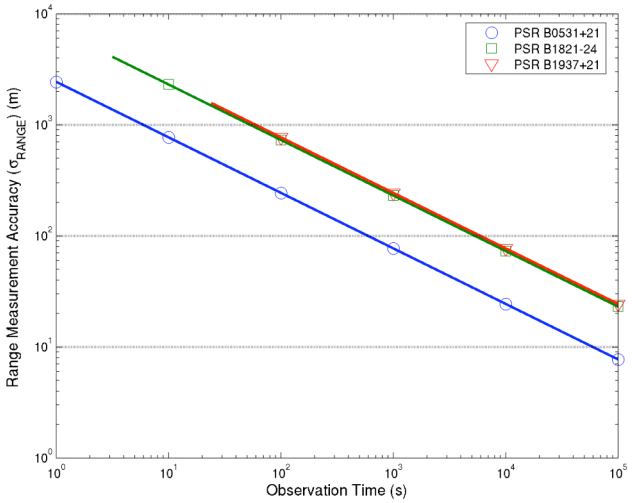

Figure 2. Range accuracy of three pulsars.

Table 3. Range Measurement Accuracy For Three Pulsars (1-m^2 Detector).

Name (PSR)	σ_{range} Range Measurement Accuracy (m)		
	500 s Observ.	1000 s Observ.	5000 s Observ.
B1937+21	344	247	110
B1821–24	325	233	104
B0531+21	109	77.9	34.8

VEHICLE STATE DYNAMICS

The states used to describe the spacecraft dynamics are the three-dimensional inertial frame position and velocity. The state vector, $\mathbf{x}$, has a total of six states, and is composed of the three element position vector, $\mathbf{r} = \mathbf{r}_{SC} = \{r_x, r_y, r_z\}^T$, and the three element velocity vector, $\mathbf{v} = \mathbf{v}_{SC} = \{v_x, v_y, v_z\}^T$. Thus, the states are represented in vector form as,

$$\mathbf{x} = \begin{bmatrix} \mathbf{r} \\ \mathbf{v} \end{bmatrix} \tag{7}$$

The dynamics of a non-linear system can be represented using the state vector as,

$$\dot{\mathbf{x}}(t) = \vec{f}\left(\mathbf{x}(t), t\right) + \boldsymbol{\eta}(t) \tag{8}$$

In this equation, $\vec{f}$ is a non-linear function of the state vector, and perhaps time. The second term in Eq. (8) is the noise vector associated with the state dynamics. With vehicle acceleration, $\mathbf{a}$, being the time derivative of velocity, velocity the time derivative of position, and ignoring noise, the time derivative of the state vector from Eq. (7) can be represented as,

$$\dot{\mathbf{x}} = \vec{f}\left(\mathbf{x}(t), t\right) = \begin{bmatrix} \dot{\mathbf{r}} \\ \dot{\mathbf{v}} \end{bmatrix} = \begin{bmatrix} \mathbf{v} \\ \mathbf{a} \end{bmatrix} \tag{9}$$

Once an initial condition is known, as,

$$\mathbf{x}(t_0) = \mathbf{x}_0 = \begin{bmatrix} \mathbf{r}_0 \\ \mathbf{v}_0 \end{bmatrix} \tag{10}$$

and the acceleration on the vehicle is computed, the state dynamics of Eqs. (9) and (10) completely defines the motion of the spacecraft.

If an analytical expression for the integral of Eq. (9) can be determined, then the vehicle state can be computed analytically at future time, t. However, the full dynamics of a spacecraft is complex due to multiple high order effects, and accurate analytical solutions are difficult to produce. Thus, the dynamics of the spacecraft, along with its initial condition, are typically numerically integrated in order to determine the vehicle's future state.

The six translational state elements of position and velocity of a spacecraft in Eq. (7) is one possible

representation for the dynamics. An alternative method is the utilization of *Keplerian* elements that describe a specific orbit of a spacecraft [20]. An advantage to this representation is that except for time within the orbit the remaining five classical Keplerian elements are nearly constant, and once determined to high accuracy can define a vehicle's orbit with high performance. However, a significant disadvantage of using Keplerian elements as state variables is that these elements are only valid for one specific orbit. This may be useful for a spacecraft that is launched and placed in a set orbit, with no mission operations deviating from that orbit. However, if a spacecraft's mission requires it to maneuver at some point, by merely changing its position along the track of its orbit or possibly altering its entire orbit shape, the six inertial states of position and velocity are much more suitable for these types of mission operations. Also, if a vehicle does not operate along a definable Keplerian orbit, the position and velocity states are more appropriate for this motion. An example of this motion is a group of spacecraft flying in formation, where the leader is in a Keplerian orbit, but its followers must maintain non-Keplerian orbits to remain in the desired formation.

To adequately represent a spacecraft's orbit about a central body, the following acceleration effects are considered for this analysis: central two-body acceleration effects; non-spherical gravitational potential effects from the central body; atmospheric drag effects if the spacecraft is close to the central body's atmosphere; and any appreciable third-body gravitational potential effects [21, 22]. The total acceleration on a spacecraft orbiting Earth is the sum of these effects as,

$$\begin{aligned}\mathbf{a}_{total} = \ddot{\mathbf{r}} = \mathbf{a}_{two-body} + \mathbf{a}_{non-spherical} + \mathbf{a}_{drag} \\ + \mathbf{a}_{Sun} + \mathbf{a}_{Moon} + \mathbf{a}_{H.O.T}\end{aligned} \tag{11}$$

In this equation, $\mathbf{a}_{H.O.T}$ represents all *higher-order terms* that may affect acceleration (such as solar radiation pressure, vehicle thrusters, etc.) but are nominally considered negligible compared to the remaining effects.

NAVIGATION KALMAN FILTER

Using the dynamics presented above, estimates of the spacecraft's flight path can be generated over time. Unforeseen disturbances or unmodeled effects eventually reduce the accuracy of these estimates. Blending pulsar-based range measurements with the vehicle dynamics provides a method to continually correct any errors within the state estimates. A navigation Kalman filter (NKF) is presented here to accomplish the integration of the dynamics and the measurement processing.

The NKF is implemented as an *extended* Kalman filter, due to the non-linear state dynamics. The states of this filter are the errors within the state vector. These error-states, $\delta\mathbf{x}$, can be represented based upon the true states, $\mathbf{x}$, and the estimated states, $\tilde{\mathbf{x}}$, as,

$$\mathbf{x} = \tilde{\mathbf{x}} + \delta\mathbf{x} \tag{12}$$

Necessary for error-state and error-covariance processing within the NKF is the proper representation of the state transition matrix, $\boldsymbol{\Phi}$. This matrix is used to determine the values of the error-state at a future time, t.

$$\delta\mathbf{x} = \boldsymbol{\Phi}(t, t_0)\,\delta\mathbf{x}_0 \tag{13}$$

The state transition matrix is found by solving the integral of the following expressions,

$$\begin{aligned}\dot{\boldsymbol{\Phi}}(t, t_0) &= \mathbf{F}(t)\boldsymbol{\Phi}(t, t_0) \\ \boldsymbol{\Phi}(t_0, t_0) &= \mathbf{I}\end{aligned} \tag{14}$$

The Jacobian matrix, $\mathbf{F}(t)$, is defined as the derivative of the dynamics of the states with respect to it states, as in,

$$\mathbf{F}(t) = \frac{\partial \bar{f}(\tilde{\mathbf{x}})}{\partial \mathbf{x}} = \frac{\partial}{\partial \mathbf{x}}\begin{bmatrix}\mathbf{v} \\ \mathbf{a}\end{bmatrix} = \begin{bmatrix}\dfrac{\partial \mathbf{v}}{\partial \mathbf{r}} & \dfrac{\partial \mathbf{v}}{\partial \mathbf{v}} \\ \dfrac{\partial \mathbf{a}}{\partial \mathbf{r}} & \dfrac{\partial \mathbf{a}}{\partial \mathbf{v}}\end{bmatrix} \tag{15}$$

From the definition of the states of Eqs. (7) and (9), the first row elements of Eq. (15) can be simplified as,

$$\frac{\partial \mathbf{v}}{\partial \mathbf{r}} = \mathbf{0}_{3x3};\ \frac{\partial \mathbf{v}}{\partial \mathbf{v}} = \mathbf{I}_{3x3} \tag{16}$$

The second row elements depend entirely upon the acceleration of the spacecraft, and cannot be immediately simplified. Thus, using Eq. (16), the Jacobian matrix for spacecraft dynamics can be expressed as,

$$\mathbf{F}(t) = \begin{bmatrix}\mathbf{0}_{3x3} & \mathbf{I}_{3x3} \\ \dfrac{\partial \mathbf{a}}{\partial \mathbf{r}} & \dfrac{\partial \mathbf{a}}{\partial \mathbf{v}}\end{bmatrix} \tag{17}$$

Using the representations for the partial derivatives of acceleration the terms for the Jacobian matrix in Eq. (17) can be assembled as [21, 22],

$$\frac{\partial \mathbf{a}}{\partial \mathbf{r}} = \frac{\partial \mathbf{a}_{two-body}}{\partial \mathbf{r}} + \frac{\partial \mathbf{a}_{non-spherical}}{\delta \mathbf{r}} + \frac{\partial \mathbf{a}_{drag}}{\partial \mathbf{r}} + \sum_{i=1}^{SS} \frac{\partial \mathbf{a}_{i^{th}\ third-body}}{\partial \mathbf{r}} \tag{18}$$

$$\frac{\partial \mathbf{a}}{\partial \mathbf{v}} = \frac{\partial \mathbf{a}_{drag}}{\partial \mathbf{v}} \tag{19}$$

In Eq. (18), the third-body gravitational potential effects are summed over all the bodies within the solar system (*SS*). In the NKF, only the Moon and Sun are considered for Earth-orbiting spacecraft. Drag is the only perturbing force that is a function of velocity, thus the only term in Eq. (19). Only estimated values are considered in this matrix, such that $\mathbf{F} = \mathbf{F}(\tilde{\mathbf{r}}, \tilde{\mathbf{v}})$. This matrix can be used in the numerical integration of Eq. (14) in order to determine the current state transition matrix used for time propagation of the error-states and error-covariances.

The expectations of the error-states and the noise of the k^{th} step in a discrete system are represented as,

$$\mathbf{P}_k = E\left[\delta\mathbf{x}_k \delta\mathbf{x}_k^T\right] \tag{20}$$

$$\mathbf{Q}_k = E\left[\boldsymbol{\eta}_k \boldsymbol{\eta}_k^T\right] \tag{21}$$

The *covariance matrix*, $\mathbf{P}$, is symmetric and provides a representation of the statistical uncertainty in the error-states, $\delta\mathbf{x}$ [23]. The $\mathbf{Q}$ matrix is referred to as the *process noise* matrix for the system, and is related to how well the dynamics of the state variables are known. The NKF interprets high process noise as poor knowledge of the dynamics. The noise of the individual states, $\boldsymbol{\eta}$, is assumed to be uncorrelated with respect to time (*white noise*), and assumed to be uncorrelated with respect to the states such that $E\left[\delta\mathbf{x}_k \boldsymbol{\eta}_k^T\right] = \mathbf{0}$. The discrete form of the dynamics of the covariance matrix can be represented as [23],

$$\mathbf{P}_{k+1}^- = \boldsymbol{\Phi}_k \mathbf{P}_k \boldsymbol{\Phi}_k^T + \boldsymbol{\Gamma}_k \mathbf{Q}_k \boldsymbol{\Gamma}_k^T \tag{22}$$

From the dynamics of Eq. (8), the matrix $\boldsymbol{\Gamma}$ is identity. Eqs. (13) and (22) represent the *time update* (*a priori*) of the NKF.

Similar to the state dynamics, the observations may also have a non-linear relationship with respect to the whole-value states. Thus the measurement, $\mathbf{y}$, has the following representation,

$$\mathbf{y}(t) = \vec{h}\left(\mathbf{x}(t), t\right) + \boldsymbol{\nu}(t) \tag{23}$$

In this expression, $\vec{h}$ is a non-linear function of the state vector, and perhaps time. The measurement noise associated with each observation is represented as $\boldsymbol{\nu}$.

In order to assemble the observations in terms of the error-states of the NKF, a measurement difference, $\mathbf{z}$, between the measurement and its estimate from Eq. (23) is computed [23]. To first order, this difference is computed as,

$$\begin{aligned}\mathbf{z}(t) &= \mathbf{y}(t) - \vec{h}\left(\tilde{\mathbf{x}}\right) = \frac{\partial \vec{h}\left(\tilde{\mathbf{x}}\right)}{\partial \mathbf{x}} \delta\mathbf{x} + \boldsymbol{\nu}(t) \\ &= \mathbf{H}\left(\tilde{\mathbf{x}}\right)\delta\mathbf{x} + \boldsymbol{\nu}(t)\end{aligned} \tag{24}$$

This measurement difference, $\mathbf{z}(t)$, is referred to as the *measurement residual*, and $\mathbf{H}$ is the *measurement matrix* of measurement partial derivatives with respect to the states [23]. This can be represented in discrete form as,

$$\mathbf{z}_{k+1} = \mathbf{H}_{k+1}\delta\mathbf{x}_{k+1} + \boldsymbol{\nu}_{k+1} \tag{25}$$

The optimal Kalman gain, $\mathbf{K}_{opt}$, can be computed based upon the time update of the covariance matrix, the measurement matrix, and the expectations of the measurement noise, $\mathbf{R} = E\left[\boldsymbol{\nu}\boldsymbol{\nu}^{\mathbf{T}}\right]$ [24]. In discrete form this is written as,

$$\mathbf{K}_{k+1_{opt}} = \mathbf{P}_{k+1}^- \mathbf{H}_{k+1}^T \left(\mathbf{H}_{k+1}\mathbf{P}_{k+1}^- \mathbf{H}_{k+1}^T + \mathbf{R}_{k+1}\right)^{-1} \tag{26}$$

Utilizing this optimal gain, the *measurement update* (*a posteriori*) of the state estimates and the covariance matrix are produced as [23, 25],

$$\tilde{\mathbf{x}}_{k+1}^+ = \tilde{\mathbf{x}}_{k+1}^- + \mathbf{K}_{k+1_{opt}} \mathbf{z}_{k+1} \tag{27}$$

$$\mathbf{P}_{k+1}^+ = \left(\mathbf{I} - \mathbf{K}_{k+1_{opt}} \mathbf{H}_{k+1}\right)\mathbf{P}_{k+1}^- \tag{28}$$

Although most observations, or measurements, are assumed valid, spurious or erroneous measurements may occur due to sensor malfunction or data processing issues. If erroneous pulsar-based measurements are improperly labeled with a low measurement noise, the processing of these erroneous measurements through the Kalman filter can severely impact the filter's performance. Therefore, is prudent to test individual measurements prior to their incorporation into the filter to avoid these negative situations. Individual measurements are tested using the filter's own estimate of its performance to evaluate a measurement. Once the filter processes enough measurements and the state covariance has been reduced from its initial condition, any out-lying measurements that are many times the filter's estimate of its performance can be ignored. The *innovations* of the filter are determined from the optimal Kalman gain calculations of Eq. (26) [23]. For non-linear systems, this innovations term, $\boldsymbol{\alpha}$, is,

$$\boldsymbol{\alpha}_{k+1} = \mathbf{H}_{k+1}\mathbf{P}_{k+1}^- \mathbf{H}_{k+1}^T + \mathbf{R}_{k+1} \tag{29}$$

Assuming N individual states, an individual scalar measurement from Eq. (25) can be represented as,

$$z_i = \mathbf{H}\left(i, 1:N\right)\delta\mathbf{x}_{Nx1} \tag{30}$$

The innovations for this measurement are the i^{th} diagonal element of Eq. (29), as $\alpha_i = \boldsymbol{\alpha}_{k+1}\left(i,i\right)$. An individual measurement is compared to its innovations as,

$$z_i \le m\alpha_i \tag{31}$$

The scalar m is the proportional value of the innovations chosen as an acceptable limit for the test. As long as the measurement is m-times less than the filter's innovations, the filter processes the measurement. Typical values of m are between 3 and 5, and the NKF uses 5. Eq. (31) is referred to as the *measurement residual test*.

MEASUREMENT MODELS

The NKF utilizes range measurements produced by the observation of pulses from pulsars. The range measurement for spacecraft relative to a reference location is produced by comparing the measured pulse TOA at the spacecraft to its predicted TOA at the reference location. Any difference in the measured and predicted TOA values is assumed to be a result of errors in the estimated vehicle position.

If not located at the SSB, a spacecraft sensor will detect a pulse at a time relative to the predicted time based upon the model of Eq. (3). A direct comparison of the arrival time at the spacecraft to the same pulse's arrival time at

the SSB is accomplished using time transfer equations. These equations require knowledge of the spacecraft's position and velocity in order to be implemented correctly. In the NKF's measurement scheme, estimated values of spacecraft position and velocity are utilized within the time transfer equation to create the best estimates of pulse arrival times at the SSB. These state estimates are provided by the onboard orbit propagator of Eqs. (9) and (10) implemented within the vehicle's navigation system, which provides a continuous estimate of the vehicle's dynamics during a pulsar observation.

Figure 3 presents a diagram of an Earth-orbiting spacecraft and a distant pulsar. The pulse model is defined at the SSB, which is located very near the Sun's surface. Unit direction to the pulsar is shown as well as the position of the spacecraft with respect to the SSB, $\mathbf{r}_{SC}$, the position of Earth with respect to the SSB, $\mathbf{r}_E$, and the position of the spacecraft with respect to Earth, $\mathbf{r}_{SC/E}$.

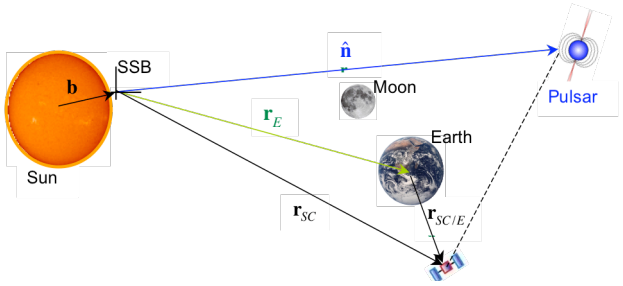

Figure 3. Pulsar viewed by Earth-orbiting spacecraft.

To first order, the pulse TOA measured at the spacecraft, t_{SC}, can be transferred to its corresponding time at the SSB, t_b, via the geometry of Figure 3. Using c for speed of light and $\hat{\mathbf{n}}_i$ for unit direction to the i^{th} pulsar, the transfer is simply [10, 11],

$$t_b = t_{SC} + \frac{\hat{\mathbf{n}}_i \cdot \mathbf{r}_{SC}}{c} \tag{32}$$

The transfer equation can also be computed with the spacecraft's position relative to Earth, using the known Earth position as,

$$t_b = t_{SC} + \frac{\hat{\mathbf{n}}_i}{c} \cdot \left(\mathbf{r}_E + \mathbf{r}_{SC/E} \right) \tag{33}$$

Earth's position with respect to the SSB can be provided by standard ephemeris tables (ex. JPL ephemeris data).

The NKF is used to determine the errors of the spacecraft position and velocity. Using the estimated value of this position, $\tilde{\mathbf{r}}_{SC/E}$, the error in this value, $\delta\mathbf{r}_{SC/E}$, is related to the true value as,

$$\mathbf{r}_{SC/E} = \tilde{\mathbf{r}}_{SC/E} + \delta\mathbf{r}_{SC/E} \tag{34}$$

Therefore, the time transfer relationship in Eq. (33) can be written in terms of the position error as,

$$ct_b = \left[ct_{SC} + \hat{\mathbf{n}}_i \cdot \left(\mathbf{r}_E + \tilde{\mathbf{r}}_{SC/E} \right) \right] + \hat{\mathbf{n}}_i \cdot \delta\mathbf{r}_{SC/E} \tag{35}$$

Eq. (35) is in the form of the Kalman filter measurement equation of Eq. (24), where,

$$\begin{aligned} \mathbf{y} &= ct_b \\ \vec{h}\left(\tilde{\mathbf{x}}\right) &= ct_{SC} + \hat{\mathbf{n}}_i \cdot \left(\mathbf{r}_E + \tilde{\mathbf{r}}_{SC/E} \right) \\ \mathbf{z} &= \mathbf{y} - \vec{h}\left(\tilde{\mathbf{x}}\right) = ct_b - \left[ct_{SC} + \hat{\mathbf{n}}_i \cdot \left(\mathbf{r}_E + \tilde{\mathbf{r}}_{SC/E} \right) \right] \\ \mathbf{H}\left(\tilde{\mathbf{x}}\right)\delta\mathbf{x} &= \hat{\mathbf{n}}_i \cdot \delta\mathbf{r}_{SC/E} \end{aligned} \tag{36}$$

The observation, $\mathbf{y}$, is the predicted TOA from the pulse timing model of Eq. (3) of the pulse nearest the measurement $\vec{h}\left(\tilde{\mathbf{x}}\right)$.

Although the first order measurement of Eq. (36) represents the conceptual implementation of a pulsar-based range equation, additional higher order terms should be included in order to accurately transfer time from a spacecraft to the SSB. Special and General relativity theorize effects on the propagation of the pulsar pulse wave as it travels from a pulsar, through the solar system, past the spacecraft, and on to the SSB. One is the effect of relativistic time transfer due to path bending within the solar system that should be included to adjust the pulse arrival time calculation. The second is the effect of a clock, which is used to time the pulse arrivals, that is in motion relative to a fixed inertial frame clock. This *proper time* to *coordinate time* correction of the spacecraft clock's time measurement must account for the vehicle's motion and gravitational effects from nearby bodies.

Using the coordinate time of the pulse TOA at the spacecraft, t_{SC}, the relativistic effects introduce the proper-motion of the pulsar, $\mathbf{V}$, which changes the pulsar's position from its initial location of $\mathbf{D}_0$ at the transmission of the 0^{th} pulse, t_0, to the transmission of the N^{th} pulse at t_N $\left(\Delta t_N \cong t_N - t_0\right)$. Also considered is the position of the SSB relative to the Sun, $\mathbf{b}$. Assuming the sun is the primary gravitational potential, μ_{Sun}, affecting the photon path, and assuming terms of $O\left(1/D_0^2\right)$ are negligible, the following time transfer equation results [11, 26],

$$\begin{aligned} t_b = t_{SC} + \frac{1}{c}\Bigg[& \hat{\mathbf{n}}_i \cdot \mathbf{r}_{SC} - \frac{r_{SC}^2}{2D_0} + \frac{\left(\hat{\mathbf{n}}_i \cdot \mathbf{r}_{SC}\right)^2}{2D_0} + \frac{\mathbf{r}_{SC} \cdot \mathbf{V}\Delta t_N}{D_0} \\ & - \frac{\left(\hat{\mathbf{n}}_i \cdot \mathbf{V}\Delta t_N\right)\left(\hat{\mathbf{n}}_i \cdot \mathbf{r}_{SC}\right)}{D_0} - \frac{\left(\mathbf{b} \cdot \mathbf{r}_{SC}\right)}{D_0} \\ & + \frac{\left(\hat{\mathbf{n}}_i \cdot \mathbf{b}\right)\left(\hat{\mathbf{n}}_i \cdot \mathbf{r}_{SC}\right)}{D_0} \Bigg] \\ & + \frac{2\mu_{Sun}}{c^3} \ln \left| \frac{\hat{\mathbf{n}}_i \cdot \mathbf{r}_{SC} + r_{SC}}{\hat{\mathbf{n}}_i \cdot \mathbf{b} + b} + 1 \right| \end{aligned} \tag{37}$$

The non-linear terms in this expression with respect to vehicle position, $\mathbf{r}_{SC}$, can be linearized about the position

error, $\delta\mathbf{r}_{SC/E}$. Assuming second-order and higher terms involving position error are negligible, this expression can be put into the Kalman filter measurement form as,

$$\mathbf{y} = ct_b$$

$$\vec{h}(\tilde{\mathbf{x}}) = ct_{SC} + (\hat{\mathbf{n}}_i \cdot \tilde{\mathbf{r}}_{SC}) + \frac{1}{D_0}\begin{bmatrix} \frac{1}{2}(\hat{\mathbf{n}}_i \cdot \tilde{\mathbf{r}}_{SC})^2 - \frac{1}{2}\tilde{r}_{SC}^2 \\ +(\tilde{\mathbf{r}}_{SC} \cdot \mathbf{V}\Delta t_N) \\ -(\hat{\mathbf{n}}_i \cdot \mathbf{V}\Delta t_N)(\hat{\mathbf{n}}_i \cdot \tilde{\mathbf{r}}_{SC}) \\ -(\mathbf{b} \cdot \tilde{\mathbf{r}}_{SC}) \\ +(\hat{\mathbf{n}}_i \cdot \mathbf{b})(\hat{\mathbf{n}}_i \cdot \tilde{\mathbf{r}}_{SC}) \end{bmatrix}$$

$$+\frac{2\mu_{Sun}}{c^2}\ln\left|\frac{\hat{\mathbf{n}}_i \cdot \tilde{\mathbf{r}}_{SC} + \tilde{r}_{SC}}{\hat{\mathbf{n}}_i \cdot \mathbf{b} + b} + 1\right| \qquad (38)$$

$$\mathbf{z} = \mathbf{y} - \vec{h}(\tilde{\mathbf{x}})$$

$$\mathbf{H}(\tilde{\mathbf{x}})\delta\mathbf{x} = \begin{bmatrix} \hat{\mathbf{n}}_i + \frac{1}{D_0}\begin{bmatrix} (\hat{\mathbf{n}}_i \cdot \tilde{\mathbf{r}}_{SC})(\hat{\mathbf{n}}_i) - \tilde{\mathbf{r}}_{SC} \\ +(\mathbf{V}\Delta t_N) - (\hat{\mathbf{n}}_i \cdot \mathbf{V}\Delta t_N)(\hat{\mathbf{n}}_i) \\ -\mathbf{b} + (\hat{\mathbf{n}}_i \cdot \mathbf{b})(\hat{\mathbf{n}}_i) \end{bmatrix} \\ +\frac{2\mu_{Sun}}{c^2}\left[\frac{\hat{\mathbf{n}}_i + (\tilde{\mathbf{r}}_{SC}/\tilde{r}_{SC})}{(\hat{\mathbf{n}}_i \cdot \tilde{\mathbf{r}}_{SC} + \tilde{r}_{SC}) + (\hat{\mathbf{n}}_i \cdot \mathbf{b} + b)}\right] \end{bmatrix}^T \delta\mathbf{r}$$

This representation assumes a TOA measurement from a recognizable singular source. Additional complexity is added if binary pulsar observations are incorporated, and these extra terms must be considered within the time transfer equations [27].

The coordinate time used for the spacecraft observation time in the above equations is composed of the spacecraft's accurate clock time, or proper time, τ_{SC}, and the standard corrections from this proper time to standard coordinate time [28]. Spacecraft clocks must also be corrected for their motion within the inertial fame. Therefore, the coordinate time of spacecraft orbiting Earth can be represented as [11, 29],

$$t_{SC} = \tau_{SC} + StdCorr_E + \frac{1}{c^2}(\mathbf{v}_E \cdot \mathbf{r}_{SC/E}) \qquad (39)$$

For spacecraft using an estimated position, the spacecraft's position relative to Earth can be represented by its estimate and its error, and the coordinate time equation from Eq. (39) becomes,

$$t_{SC} = \tau_{SC} + StdCorr_E + \frac{1}{c^2}(\mathbf{v}_E \cdot \tilde{\mathbf{r}}_{SC/E}) + \frac{1}{c^2}(\mathbf{v}_E \cdot \delta\mathbf{r}_{SC/E}) \qquad (40)$$

This expression for spacecraft coordinate time could be incorporated into the NKF measurement of Eq. (38). For some applications, adding clock error and clock rate error to the state vector within the NKF would allow estimation of spacecraft clock drift. Various models could be used for the clock error state dynamics, some similar to the implementations used for GPS receiver clock error analysis [25]. Eq. (40) assumes no error in the coordinate time standard corrections, Earth inertial velocity, $\mathbf{v}_E$, or Earth ephemeris data, however, these errors could also be include if considered relevant.

VISIBILITY OBSTRUCTION

Even though sources are very distant from the solar system, any body that passes between the spacecraft and the source may obstruct a spacecraft detector's view of the source. To avoid this obstruction occurring during a planned source observation, it is necessary to determine the locations within an orbit where the detector's visibility of a source is obstructed. Any source that is not perpendicular to the vehicle's orbit plane may pass behind Earth's limb for some portion of the orbit.

Figure 4 provides a diagram of a spacecraft in Earth orbit, as well as the shadow on the orbit cast by Earth. Earth will block the view of the source while the vehicle is in the shadow. Any celestial body, other spacecraft, or components on the vehicle itself could obscure the view of a source. The size of an object and its distance from the spacecraft's detector affects the amount of obscuration. If a celestial body has an appreciable atmosphere, which may absorb X-ray photons, this height of the atmosphere must be added to the diameter of the body when determining source visibility.

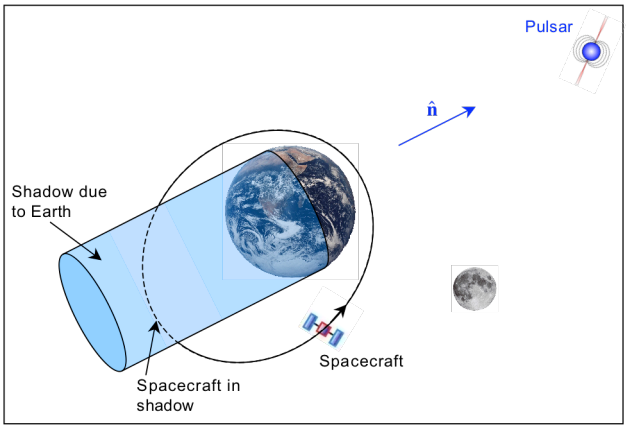

Figure 4. Shadow of pulsar cast by Earth on spacecraft orbit.

To determine whether a planetary body obscures the view of a source, it is necessary to determine the size of the shadow cast by the body and whether the spacecraft's path intersects this shadow [30]. Figure 5 provides a diagram of the orbit of a vehicle about this body and the geometry associated with the shadow cast by the body. The angle, ψ, between the vehicle's position relative to the body, $\mathbf{r}_{SC/B}$, and the unit direction to the source, $\hat{\mathbf{n}}$, can be determined from,

$$\cos(\psi) = \hat{\mathbf{n}} \cdot \mathbf{r}_{SC/B} \qquad (41)$$

The vehicle is within the body's shadow when this angle is between the entrance and exit angles, ψ_{ENT} and ψ_{EXIT} respectively, of the shadow,

$$\psi_{ENT} \le \psi \le \psi_{EXIT} \tag{42}$$

From the geometry based upon the radius of the body, $\mathbf{R}_B$, these angles can be expressed using source direction and spacecraft position as [30],

$$\pi - \arccos\left(\frac{\sqrt{r_{SC/B}^2 - R_B^2}}{r_{SC/B}}\right) \le \arccos\left(\hat{\mathbf{n}} \cdot \mathbf{r}_{SC/B}\right) \le \pi + \arccos\left(\frac{\sqrt{r_{SC/B}^2 - R_B^2}}{r_{SC/B}}\right) \tag{43}$$

If the computed angle is between these bounds, then the vehicle is within the body's shadow. For Earth, the planetary radius should include Earth's atmosphere height, h_{ATM}, such that $R_B = R_E + h_{ATM}$.

Using the Crab pulsar data from Table 1 and the orbit of the ARGOS vehicle with Eq. (43), this pulsar is visible for approximately 4317 s during the 6102 s orbital period. Figure 6 plots the visibility of the Crab pulsar, in addition to PSR B1937+21 and PSR B1821+24 during four ARGOS orbits due to the combined effects of the shadows of Earth, the Sun, and the Moon. This figure shows that at least one pulsar is visible during each of these orbits. Although visibility durations for a specific source can be determined using this method along a spacecraft orbit, additional visibility limitations such as vehicle component obstruction or detector gimbaled axis limitations may reduce these durations. Similar analysis has been completed for visibility of these three pulsars in the GPS orbit. Although the GPS satellite nearly enters Earth's shadow for the Crab pulsar, all three pulsars are visible for the entire orbit of this satellite.

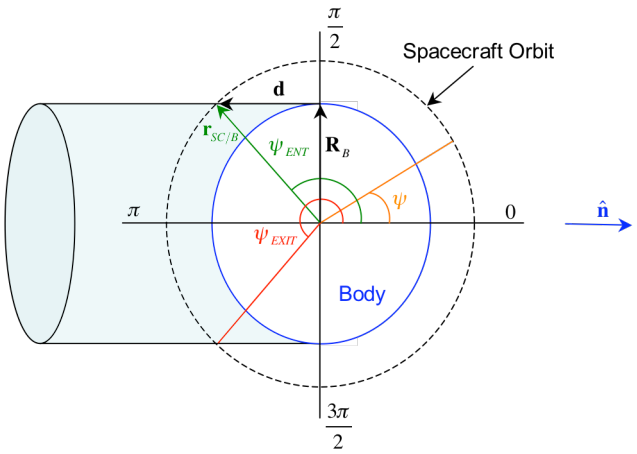

Figure 5. Geometry of body shadow on orbit.

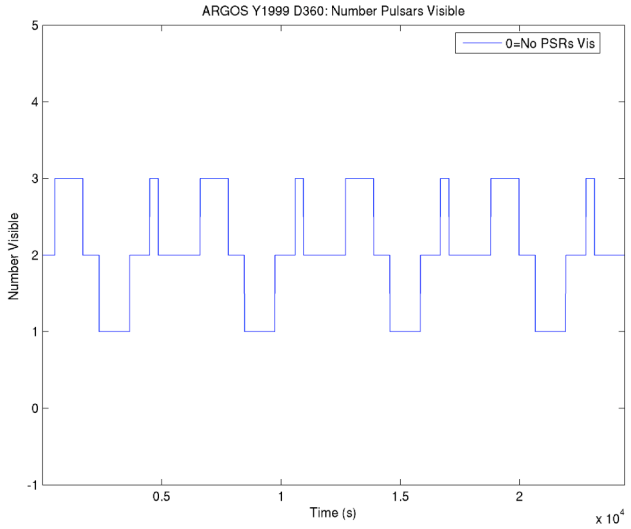

Figure 6. Visibility of three pulsars due to shadows from Earth, Sun, and Moon in ARGOS orbit.

SIMULATION AND RESULTS

To test the performance of the NKF, a simulation was developed that incorporates vehicle dynamics and pulsar-based range measurements. The vehicle state dynamics was implemented as in Eqs. (9) and (10). The non-spherical Earth gravitational zonal terms of J_2 through J_6 were implemented [21], and a Harris-Priester model of Earth's atmosphere was utilized [22]. The Moon and Sun were the two third-body effects considered. The solar system position and velocity information was provided by the JPL ephemeris data [31].

Three existing satellite orbits of ARGOS, Laser Geodynamics (LAGEOS-1), and GPS Block IIA-16 PRN-01 were investigated. Initial truth state conditions were chosen from the two-line element sets (TLE) of orbit data provided by NORAD [32]. These TLE sets are read by analytical perturbation orbit propagators (SGP4) [33]. The TLE data provide the ballistic coefficients of the spacecraft used in the atmospheric drag computations. A proposed orbit of the Lunar Reconnaissance Orbiter (LRO) was also investigated. This planned mission will orbit the Moon at an altitude of 50 km beginning in 2008.

The simulated state dynamics for these orbits was integrated using a fourth-order Runge-Kutta method with a fixed time step of 10 s. The resulting solution was verified using both the TLE SGP4 and the NRL PPT3 [34] analytical orbit propagators. During the state integration, the state transition matrix, $\mathbf{\Phi}$, was simultaneously computed.

The vehicle state estimate and transition matrix were provided to the NKF to process a time-update of the covariance matrix. The initial standard deviations for the covariance matrix were chosen as $\sigma_{\delta \mathbf{r}_0}$ = 250 m and $\sigma_{\delta \mathbf{v}_0}$

= 0.25 m/s for each axis [22]. The one-sigma state process noise was chosen as $\eta_{\delta \mathbf{r}}$ = 0.05 m and $\eta_{\delta \mathbf{v}}$ = 0.05 mm/s, and assumed fixed for the entire simulation run [22].

Pulsar-based range measurements were simulated using the relativistic time transfer and measurement of Eq. (38). The measurement noise, $\boldsymbol{\nu}(t)$, associated with Eq. (38) was simulated as random with a standard deviation equal to the range accuracy of each pulsar based upon the results of Table 3, assuming an 1-m^2 detector. The relativistic time transfer and measurement were computed assuming spacecraft coordinate time, although the effects of proper time to coordinate time conversion of Eq. (40) will be incorporated in future analysis. The current analysis assumes zero pulsar proper-motion, which is small compared to the remaining terms in Eq. (38). Since some modeling error is introduced by ignoring these small effects, the measurement noise was increased by an additional 2%.

It was assumed that only one pulsar could be detected during a single fixed 500 s observation. The priority of observation was based upon the measurement accuracies from Table 3: B0531+21, B1821-24, and B1937+21. If the visibility of a pulsar was obscured during an observation, the next pulsar in the priority list was utilized. If none were available, the measurement cycle was skipped, and the successive cycle would begin.

A *truth* orbit truth model was created using a propagator with the initial conditions set from the TLE data values. The NKF used the same propagator, but had initial errors introduced to the initial conditions of the truth orbit. This requires the NKF to detect and remove these state errors based upon the simulated range measurements. All the simulated cases began with a 100 m position error and 0.01 m/s velocity error in each axis [22]. The performance of the NKF was determined by how well these errors could be detected, and by quantifying the true errors of the NKF after selected periods of operation.

Figure 7 provides a plot of the NKF's standard deviation envelope of the three axes of position for the GPS satellite orbit. The error between the true vehicle position and the NKF's estimate of position is also plotted, which remains within the one-sigma envelope after initial filter settling. Figure 8 provides a similar plot for the ARGOS orbit. Figure 9 plots the magnitude of the position error for an orbit propagation including the initial state errors but with no state corrections. It also shows the errors of the NKF solution from truth. After four GPS orbits the uncorrected state position errors has grown to ~15 km, whereas the NKF state estimate remains < 200 m after settling. Figure 10 shows after 24 ARGOS orbits, the uncorrected state errors have grown to ~ 7 km, whereas the NKF state estimate remains < 200 m.

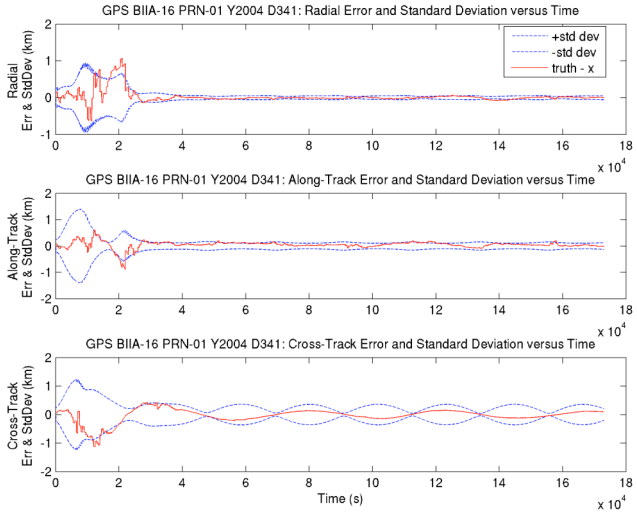

Figure 7. Standard deviation and error for GPS.

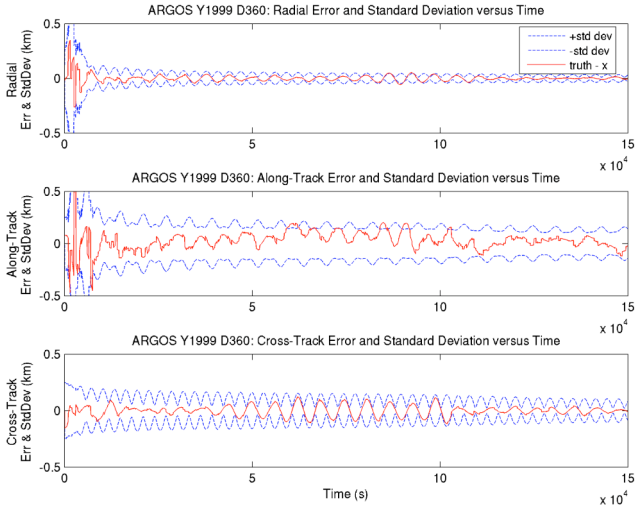

Figure 8. Standard deviation and error for ARGOS.

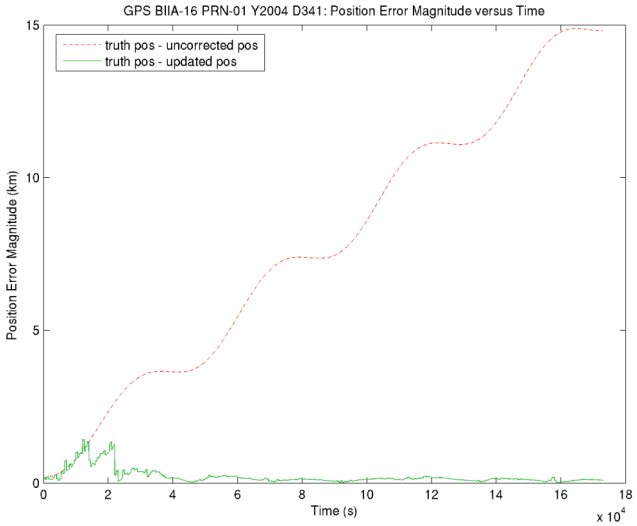

Figure 9. Uncorrected and NKF position error for GPS.

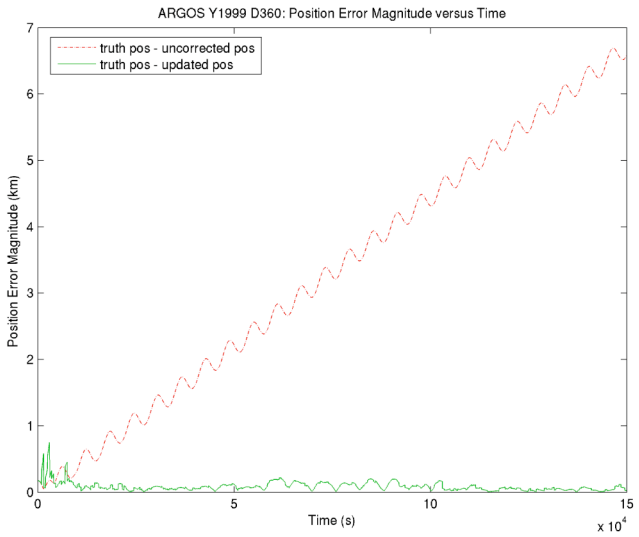

Figure 10. Uncorrected and NKF position error for ARGOS.

Table 4 provides performance values for each spacecraft orbit. The results from five separate runs with different random number seeds were averaged for this table's data. Performance values are reported for the entire simulation duration and for the duration after the initial filter settling period (usually two orbits). Data is reported in radial, along-track, and cross-track (RAC) directions of the orbit. The one-sigma errors of the filter states from truth are provided. For reference, the NKF computed covariance estimate and the error in the filter's state from truth at the end of the simulation run are provided.

For Earth-orbiting spacecraft, the performance after filter settling of the NKF is on the order of 200 m or less. Future simulations will include individual photon arrivals such that all operations are simulated to produce the range measurement and insure proper relativistic time transfer. The study of the LRO orbit is ongoing, with performance on the order of 0.5 km or less achieved. It is likely that additional filter parameter tuning is required for the LRO orbit analysis. However, the results demonstrate the potential benefits of this pulsar-based navigation system for missions above the GPS constellation orbit and for continuous operation perhaps behind the Moon, where radar contact from Earth would be unavailable.

CONCLUSIONS

Pulsars present an intriguing and unique opportunity to develop a new spacecraft navigation system. With the potential range accuracy of a few hundred meters, these sources can maintain spacecraft orbits to within 100 – 300 m (one-sigma) in three dimensions. As research on these sources and their use in navigation continues, this may allow the creation of navigation systems that produce greater autonomy for larger regions of space than existing systems alone.

Table 4. NKF Performance Values

Orbit	Sim Length (10^3 s)	1-Sigma Position Error (RAC) (m)		NKF 1-Sigma At Sim End (RAC) (m)	NKF Error At Sim End (RAC) (m)
		Full Sim Run	After filter Settling		
ARGOS	150	42 111 56	26 91 57	30 136 86	14 71 21
LAGEOS	110	74 116 201	25 57 200	15 86 147	7 69 173
GPS	173	164 154 196	23 50 90	52 129 204	20 32 62
LRO	110	359 520 371	242 401 308	290 495 245	178 309 160

ACKNOWLEDGEMENTS

The authors wish to thank the X-ray/UV Astrophysics and Applications Section at NRL, and specifically Kent Wood and Paul Ray, for their assistance in this research. They would also like to thank Glenn Creamer and Liam Healy of NRL for their helpful discussions on orbit dynamics and filter design, and Mark Beckman of NASA GSFC for LRO orbit information. Much of this research was supported with the fellowship program of the Metropolitan Washington DC Chapter of the ARCS Foundation and the Gustave J. Hokenson Fellowship of the Aerospace Engineering Department of the University of Maryland.

REFERENCES

1. Downs, G. S., "Interplanetary Navigation Using Pulsating Radio Sources," *NASA Technical Reports N74-34150*, 1974, pp. 1-12.
2. Chester, T. J., and Butman, S. A., "Navigation Using X-ray Pulsars," *NASA Technical Reports N81-27129*, 1981, pp. 22-25.
3. Wood, K. S., "Navigation Studies Utilizing The NRL-801 Experiment and the ARGOS Satellite," *Small Satellite Technology and Applications III*, Ed. B. J. Horais, International Society of Optical Engineering (SPIE) Proceedings, Vol. 1940, pp. 105-116.
4. Hewish, A., Bell, S. J., Pilkington, J. D., Scott, P. F., and Collins, R. A., "Observation of a Rapidly Pulsating Radio Source," *Nature*, Vol. 217, 1968, pp. 709-713.
5. Manchester, R. N., and Taylor, J. H., *Pulsars*, W.H. Freeman and Company, San Francisco, 1977.
6. Lyne, A. G., and Graham-Smith, F., *Pulsar Astronomy*, Cambridge University Press, 1998.

7. Matsakis, D. N., Taylor, J. H., and Eubanks, T. M., "A Statistic for Describing Pulsar and Clock Stabilities," *Astronomy and Astrophysics*, Vol. 326, 1997, pp. 924-928.
8. Kaspi, V. M., Taylor, J. H., and Ryba, M. F., "High-Precision Timing of Millisecond Pulsars. III: Long-Term Monitoring of PSRs B1855+09 and B1937+21," *Astrophysical Journal*, Vol. 428, 1994, pp. 713-728.
9. Charles, P. A., and Seward, F. D., *Exploring the X-ray Universe*, Cambridge University Press, 1995.
10. Sheikh, S. I., Pines, D. J., Wood, K. S., Ray, P. S., Lovellette, M. N., and Wolff, M. T., "The Use of X-ray Pulsars for Spacecraft Navigation," *14th AAS/AIAA Space Flight Mechanics Conference*, Paper AAS 04-109, Maui HI, February 8-12 2004.
11. Sheikh, S. I., Pines, D. J., Wood, K. S., Ray, P. S., Lovellette, M. N., and Wolff, M. T., "Spacecraft Navigation Using X-ray Pulsars," *Journal of Guidance, Control, and Dynamics*, 2005, In press.
12. Wood, K. S., Kowalski, M., Lovellette, M. N., Ray, P. S., Wolff, M. T., Yentis, D. J., Bandyopadhyay, R. M., Fewtrell, G., and Hertz, P. L., "The Unconventional Stellar Aspect (USA) Experiment on ARGOS," *American Institute of Aeronautics and Astronautics (AIAA) Space Conference and Exposition*, Albuquerque NM, August 2001.
13. Taylor, J. H., and Stinebring, D. R., "Recent Progress in the Understanding of Pulsars," *Annual Review of Astronomy and Astrophysics*, Vol. 24, 1986, pp. 285-327.
14. Taylor, J. H., "Pulsar Timing and Relativistic Gravity," *Philosophical Transactions of the Royal Society of London*, Vol. 341, 1992, pp. 117-134.
15. Fraser, G. W., *X-ray Detectors in Astronomy*, Cambridge University Press, 1989.
16. Rappaport, S., *Pulsar SNR Discussion*, Massachusetts Institute of Technology, October 2004 (personal communication).
17. Possenti, A., Cerutti, R., Colpi, M., and Mereghetti, S., "Re-examining the X-ray versus spin-down luminosity correlation of rotation powered pulsars," *Astronomy and Astrophysics*, Vol. 387, 2002, pp. 993-1002.
18. Nicastro, L., Cusumano, G., Löhmer, O., Kramer, M., Kuiper, L., Hermsen, W., Mineo, T., and Becker, W., "BeppoSAX Observation of PSR B1937+21," *Astronomy and Astrophysics*, Vol. 413, 2004, pp. 1065-1072.
19. Becker, W., and Trümper, J., "The X-ray luminosity of rotation-powered neutron stars," *Astronomy and Astrophysics*, Vol. 326, 1997, pp. 682-691.
20. Maldonado, A. L., Baylocq, M., and Hannan, G., "Autonomous Spacecraft Navigation - Extended Kalman Filter Estimation of Classical Orbital Parameters," *Guidance and Control Conference*, American Institute of Aeronautics and Astronautics (AIAA), Seattle, WA, August 20-22 1984.
21. Vallado, D. A., *Fundamentals of Astrodynamics and Applications*, Second ed., Space Technology Library, Kluwer Academic Publishers, Boston, 2001.
22. Montenbruck, O., and Gill, E., *Satellite Orbits*, Springer-Verlag, Berlin, 2000.
23. Gelb, A. Ed., *Applied Optimal Estimation*. The M.I.T. Press, Cambridge, Massachusetts, 1974.
24. Kalman, R. E., "A New Approach to Linear Filtering and Prediction Problems," *Transactions of the American Society of Mechanical Engineering - Journal of Basic Engineering*, Vol. 82, No. D, 1960, pp. 35-45.
25. Brown, R. G., and Hwang, P. Y. C., *Introduction to Random Signals and Applied Kalman Filtering*, Third ed., John Wiley and Sons, New York, 1997.
26. Hellings, R. W., "Relativistic Effects in Astronomical Timing Measurements," *Astronomical Journal*, Vol. 91, 1986, pp. 650-659.
27. Blandford, R., and Teukolsky, S. A., "Arrival-Time Analysis for a Pulsar in a Binary System," *Astrophysical Journal*, Vol. 205, 1976, pp. 580-591.
28. Seidelmann, P. K., *Explanatory Supplement to the Astronomical Almanac*, University Science Books, Sausalito CA, 1992.
29. Moyer, T. D., "Transformation from Proper Time on Earth to Coordinate Time in Solar System Barycentric Space-Time Frame of Reference - Part One," *Celestial Mechanics*, Vol. 23, 1981, pp. 33-56.
30. Escobal, P. R., *Methods of Orbit Determination*, Krieger Publishing Company, Malabar, Florida, 1965.
31. Standish, E. M., "NASA JPL Planetary and Lunar Ephemerides," [online database], NASA, URL: http://ssd.jpl.nasa.gov/eph_info.html [cited 2004].
32. Kelso, T. S., "NORAD Two-Line Element Sets Historical Archives," [online database], Celestrak, URL:http://www.celestrak.com/NORAD/archives/request.asp [cited 2004].
33. Hoots, F. R., and Roehrich, R. L., "Spacetrack Report No. 3, Model for Propagation of NORAD Element Sets," Department of Defense, Defense Documentation Center, December 1980.
34. Schumacher, P. W., and Glover, R. A., "Analytic Orbit Model for U.S. Naval Space Surveillance: An Overview," *1995 AAS/AIAA Astrodynamics Specialist Conference*, AAS Paper 95-427, American Astronautical Society, Halifax, Nova Scotia, Canada, August 14-17, 1995.